

Primordial black hole formation by vacuum bubbles

Heling Deng and Alexander Vilenkin

*Institute of Cosmology, Tufts University,
574 Boston Ave, Medford, MA, 02155 U.S.A.*

Abstract

Vacuum bubbles may nucleate during the inflationary epoch and expand, reaching relativistic speeds. After inflation ends, the bubbles are quickly slowed down, transferring their momentum to a shock wave that propagates outwards in the radiation background. The ultimate fate of the bubble depends on its size. Bubbles smaller than certain critical size collapse to ordinary black holes, while in the supercritical case the bubble interior inflates, forming a baby universe, which is connected to the exterior region by a wormhole. The wormhole then closes up, turning into two black holes at its two mouths. We use numerical simulations to find the masses of black holes formed in this scenario, both in subcritical and supercritical regime. The resulting mass spectrum is extremely broad, ranging over many orders of magnitude. For some parameter values, these black holes can serve as seeds for supermassive black holes and may account for LIGO observations.

I. INTRODUCTION

Primordial black holes (PBHs) are hypothetical black holes formed in the early universe before any nonlinear large scale structure and galaxies. The idea was conceived and developed decades ago [1–3], and since then PBHs have received considerable attention, despite the fact that their existence is yet to be supported by observations. Depending on the model, PBH masses can range from as low as the Planck mass ($M_{\text{Pl}} \sim 10^{-5}$ g) to many orders of magnitude above the solar mass ($M_{\odot} \sim 10^{33}$ g). By contrast, black holes formed by stellar collapse cannot have mass smaller than M_{\odot} . Small PBHs ($M_{\text{bh}} < 10^{15}$ g) could be sources of Hawking radiation, whereas PBHs with $M_{\text{bh}} > 10^{15}$ g have been suggested as a candidate for (at least part of) the cold dark matter and as possible seeds of supermassive black holes. Numerous mechanisms of PBH formation have been proposed over the years. In many scenarios (e.g., [4–8]), overdensity produced during inflation may overcome pressure and collapse into a black hole after it reenters the horizon during the radiation-dominated era. Other possibilities are related to first-order phase transitions [9–11], the collapse of cosmic string loops [12–14] and domain walls [14–17], etc.

In this paper, we shall use numerical simulations to explore the possibility, recently suggested in [16], that PBH could be formed by nonperturbative quantum effects in the early universe. Specifically, we will show that spontaneous nucleation of vacuum bubbles during the inflationary epoch can result in black holes with a wide mass spectrum at the present time.

The physical mechanism responsible for this phenomenon is easy to understand. The inflationary expansion of the universe is driven by the high energy density ρ_i of the false vacuum ¹. Bubble nucleation may occur by quantum tunneling if the underlying physics includes some vacuum states, other than our present vacuum, with energy density $\rho_b < \rho_i$ (we will be interested in the case where $\rho_b > 0$). A two-dimensional energy landscape corresponding to this setup is illustrated in Fig. 1. The inflaton field slowly "rolls" along the gentle slope in the landscape towards a local energy density minimum representing our vacuum. As it rolls, it can tunnel through a potential barrier to another vacuum of energy density higher than ours. The tunneling occurs through bubble nucleation: a small

¹ We use the term "false vacuum" somewhat loosely, including a slowly rolling inflaton in this category.

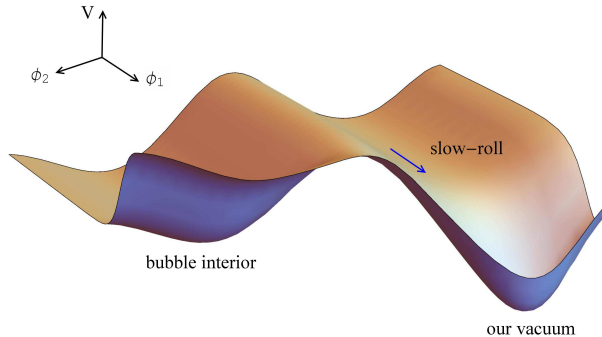


FIG. 1: A simple example of a two-field potential where the bubble nucleation scenario we discuss in this paper would be possible. As the inflaton field slowly rolls towards our vacuum, it can tunnel through a barrier to another vacuum, which will be the bubble interior.

spherical bubble of the new vacuum spontaneously forms in the inflating background [18]. Once the bubble nucleates, it expands with acceleration, acquiring a large Lorentz factor. This growth of the bubble is caused by the large vacuum tension outside (which is greater than the vacuum tension inside). At the end of inflation, the false vacuum outside the bubble decays into hot radiation. The bubble wall runs into the radiation and quickly loses much of its energy, producing a shock wave that propagates outwards. A black hole is then formed by one of the two different scenarios, depending on the size of the bubble. (i) The bubble wall is pulled inwards by the interior vacuum tension, the wall tension, as well as the radiation pressure; so it shrinks and eventually collapses to a singularity. Following [16], we shall refer to such bubbles as subcritical. (ii) If in the course of bubble expansion its size exceeds the interior de Sitter horizon, the bubble begins to inflate. In the latter case, the bubble continues to expand without bound and a wormhole is created outside the bubble wall, connecting the inflating baby universe inside and the FRW parent universe dominated by radiation. Such bubbles will be called supercritical.

It was argued in Ref. [16] that the bubble transfers most of its kinetic energy to surrounding matter and comes to rest with respect to the Hubble flow on a time scale much shorter than the Hubble time. If the exterior region were filled with pressureless dust, an empty layer would form around the bubble, so the bubble would be completely isolated from matter. In this case the bubble evolution and the mass of the resulting black hole can

be found analytically. The case with a radiation background is more involved, due to the pressure exerted on the wall. Also, if a wormhole is formed, some radiation may follow the bubble into the wormhole. Both of these effects may influence the black hole mass.

Our goal in this paper is to numerically study black hole formation by vacuum bubbles and to determine the resulting spectrum of black hole masses. The paper is organized as follows. In Section II we discuss the bubble dynamics in more detail and review some relevant earlier work. Our simulation model is described in Section III, and simulation results are presented in Section IV. We calculate the black hole mass spectrum in Section V and discuss observational implications and constraints on the model parameters in Section VI. Our conclusions are summarized and discussed in Section VII. We set $c = \hbar = 1$ throughout the paper.

II. BUBBLE DYNAMICS

We consider an idealized model where inflation ends instantaneously at time $t = t_i$, so that false vacuum outside the bubble is instantly turned into radiation of initial energy density ρ_i . We also assume, as in Ref. [16], that particles are reflected from the bubble wall, so radiation cannot penetrate the bubble and the bubble interior always remains pure de Sitter.

As we mentioned in the Introduction, the bubble evolution can lead to two possible outcomes, depending on the bubble size. We first consider subcritical bubbles.

A. Subcritical bubbles

When the bubble transfers its momentum to radiation and comes to rest with respect to the Hubble flow at $t \approx t_i$, it continues to expand by inertia. But the forces due to the tension of the vacuum inside the bubble and due to the tension of the bubble wall are both directed inwards, so the bubble wall accelerates inwards, away from the surrounding radiation, and we can expect that in a few Hubble times the interaction of the bubble with radiation becomes negligible.

In the subcritical case, the bubble eventually stops expanding and collapses to a Schwarzschild singularity; the corresponding conformal diagram is shown in Fig. 2. We

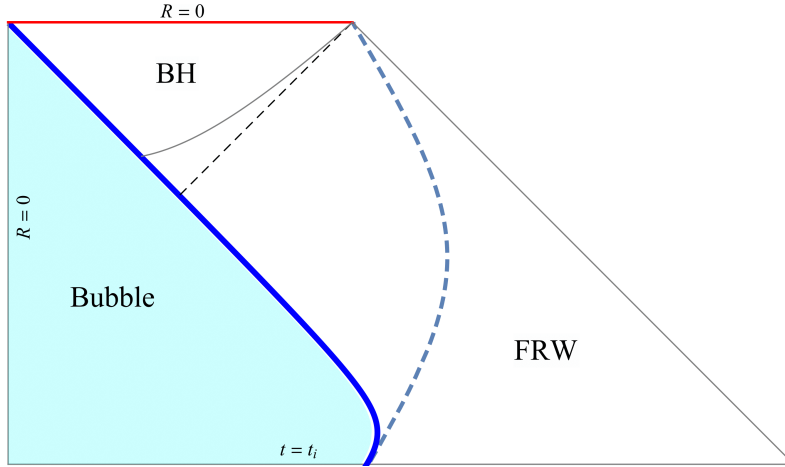


FIG. 2: A conformal diagram showing the formation of a black hole by a subcritical bubble in the background of a radiation dominated spatially flat FRW universe. At the time t_i , when inflation ends, the bubble (the shaded region of the diagram) expands with a large Lorentz factor relative to the Hubble flow. The bubble wall is represented by a thick blue solid curve. The bubble expansion is slowed down by momentum transfer to the ambient radiation, and eventually the bubble turns around and collapses into a Schwarzschild singularity (red solid line). The thick dashed curve represents the shock front propagating at the speed of sound, caused by the impact of the fast-moving wall on the radiation. Region outside the shock front is an unperturbed FRW universe. The spacelike curve below the Schwarzschild singularity is the black hole apparent horizon, which is used to represent the black hole boundary in our simulations. It lies inside the event horizon (thin dashed straight line).

can estimate the mass of the resulting black hole by assuming that the interaction with radiation is negligible right after the initial momentum transfer at $t \approx t_i$. Then the bubble dynamics is the same as it would be if the exterior region were asymptotically Minkowski. In this case the bubble can be characterized by a conserved mass parameter \mathcal{M}_b given by [19]

$$G\mathcal{M}_b = \frac{1}{2}H_b^2 R_w^3 + 2H_\sigma R_w^2 \sqrt{1 + \dot{R}_w^2 - H_b^2 R_w^2 - 2H_\sigma^2 R_w^3}, \quad (1)$$

where $R_w(\tau)$ is the bubble radius and the overdot stands for a derivative with respect to the

proper time τ on the bubble wall. We have also defined²

$$H_b = \sqrt{\frac{8\pi G \rho_b}{3}} \quad (2)$$

and

$$H_\sigma = 2\pi G \sigma, \quad (3)$$

where σ is the bubble wall tension. The first term in Eq. (1) is the interior vacuum energy of the bubble, the second term is the energy of the expanding wall, and the last term the gravitational self-energy of the wall.

Since $\mathcal{M}_b = \text{const}$, it can be evaluated at $t \approx t_i$, when $\dot{R}_w \approx H_i R_i$ with H_i the Hubble constant during inflation and R_i the bubble radius at t_i . The black hole mass is then simply $M_{\text{bh}} = \mathcal{M}_b$. Assuming that the bubble is much bigger than the horizon, $R_i \gg H_i^{-1}$, this is given by

$$GM_{\text{bh}} \approx \left[\frac{1}{2} H_b^2 + 2H_\sigma \left(\sqrt{H_i^2 - H_b^2} - H_\sigma \right) \right] R_i^3. \quad (4)$$

The maximal radius of expansion of the bubble R_{max} can be found by setting $\dot{R}_w = 0$ in Eq. (1) and solving for R_w . A solution exists only if \mathcal{M}_b is smaller than certain critical mass M_{cr} . An exact expression for M_{cr} was found in Ref. [20]; it is rather cumbersome and we will not reproduce it here. By order of magnitude, M_{cr} can be estimated as [16]

$$GM_{\text{cr}} \sim \min\{H_b^{-1}, H_\sigma^{-1}\}. \quad (5)$$

On dimensional grounds, $H_b \sim \eta_b^2/M_{\text{Pl}}$ and $H_\sigma \sim \eta_\sigma^3/M_{\text{Pl}}^2$, where η_b and η_σ are the energy scales of the interior vacuum and of the bubble wall, respectively. Then, with $\eta_b \sim \eta_\sigma \ll M_{\text{Pl}}$, we have $H_b \gg H_\sigma$ and $GM_{\text{cr}} \sim H_b^{-1}$. In this case the maximum expansion radius is related to the black hole mass as $GM_{\text{bh}} \approx H_b^2 R_{\text{max}}^3/2$. As M_{bh} is increased, R_{max} grows and reaches its largest value, $R_{\text{max}} \sim H_b^{-1}$ at the critical mass. On the other hand, a situation where $\eta_b \ll \eta_\sigma$ is also possible; then $H_\sigma \gtrsim H_b$ and $GM_{\text{cr}} \sim H_\sigma^{-1}$. The choice of parameters in our simulations was dictated mostly by the computing constraints.

We do not expect the estimates (1) and (4) to be very accurate. Radiation does work on the bubble while it expands (which decreases the bubble mass) and while it contracts (which increases the bubble mass). Since the radiation density is higher during the expanding phase,

² H_b is the rate of inflation in a vacuum of energy density ρ_b , and H_σ is the rate at which an isolated domain wall of tension σ would inflate due to its self-gravity.

one can expect the overall effect to be mass reduction (except in cases where the expanding phase is very short). But since the contact with radiation effectively ceases within a few Hubble times, it was suggested in [16] that Eqs. (1) and (4) should give the right order of magnitude. We shall see that this is indeed the case.

B. Supercritical bubbles

For $\mathcal{M}_b > M_{\text{cr}}$, the bubble expands to a radius greater than H_b^{-1} , and the bubble interior begins to inflate. At this point nothing can stop it from growing³. In this “supercritical” case, the bubble grows into a baby universe, which is connected to the parent universe outside by a wormhole throat. The wormhole closes up on a timescale $t \sim GM_{\text{bh}}$, and black holes of mass $M_{\text{bh}} > M_{\text{cr}}$ are formed at its two mouths. From then on, the baby universe has no impact on further evolution of the exterior FRW region. The corresponding spacetime structure was discussed in Ref. [16]; it is illustrated in the conformal diagram in Fig. 3. As emphasized in [16], wormhole formation in this spacetime does not violate any singularity theorems and does not require violation of the null energy condition.

An unusual feature of the diagram in Fig. 3 is the presence of a white hole region (marked WH), as in the Kruskal spacetime of an eternal black hole. The boundaries of black and white holes are usually defined by their event horizons, and we adopted this convention in the figure. A more physically motivated definition is to use apparent (or trapping) horizons (see e.g. Ref. [24] and references therein). We followed this approach in our simulations; see Sec. III.D for more detail.

The shock wave produced by the bubble wall propagates outwards at the speed of sound; its trajectory is shown by a dashed curve in the diagram. The region outside the shock remains unperturbed and is described by the FRW solution. On the other hand, the evolution inside the shock radius can be rather complicated. In particular, some radiation flows out of the white hole region, resulting in a decrease of the black hole mass. This can be thought of as an inverse process of radiation flowing into a black hole, which would increase the mass.

A related problem has been studied in Ref. [17], which investigated the collapse of spherical domain walls formed during inflation. In this case, inflation ends both inside and outside

³ For $H_\sigma > H_b$, the bubble wall starts inflating, due to its repulsive gravity, when its radius exceeds H_σ^{-1} . Inflation in the bubble interior begins when the wall expands to $R_w > H_b^{-1}$.

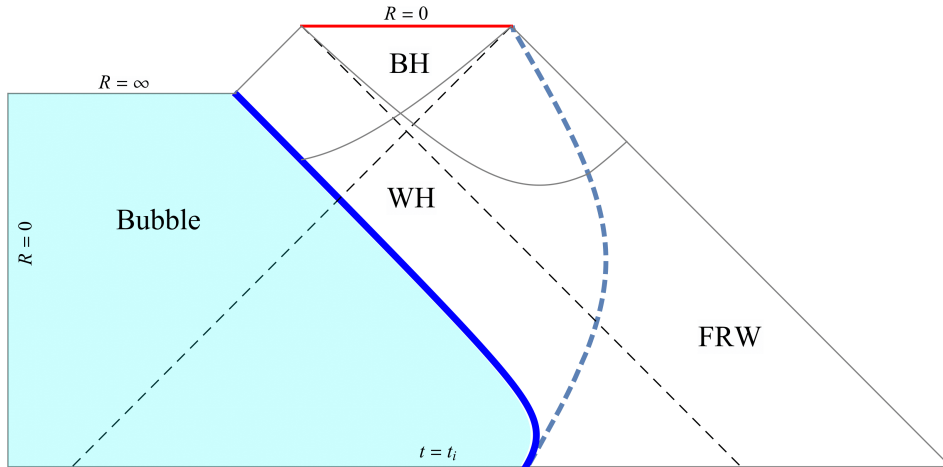


FIG. 3: A conformal diagram showing the formation of a black hole by a supercritical bubble in a radiation dominated flat FRW universe. In this case, the bubble does not collapse into a singularity. Instead, it grows exponentially in a baby universe, which is connected by a wormhole to the parent FRW universe. The thick dashed curve represents the shock front propagating at the speed of sound, caused by the interaction of the fast-moving wall and the radiation. Region outside the shock front is FRW dominated by homogeneous radiation. The two intersecting spacelike curves below the Schwarzschild singularity are the apparent horizons. The parts above the intersection are black hole apparent horizons, representing the boundary of two black holes. The right branch below the intersection goes lightlike as it approaches the FRW lightlike infinity. This null line is the Hubble radius (or cosmological apparent horizon) of the FRW universe. The two intersecting thin dashed straight lines below the apparent horizons are the event horizons.

the wall. If the wall expands to a radius greater than H_σ^{-1} , it starts inflating and a radiation-filled baby universe is formed. It was pointed out in [17] that the Schwarzschild radius of the resulting black hole cannot exceed the radius of the comoving FRW region affected by the wall when it comes within the cosmological horizon. The affected region is marked by the rarefaction wave that propagates away from the wall at the speed of sound. The resulting bound on the black hole mass is

$$GM_{\text{bh}} < 2.8H_i R_i^2. \quad (6)$$

The situation in our case is very similar, except the affected region is now bounded by the shock front. Hence we expect the same bound to apply. Numerical simulations in Ref. [17]

showed that black hole masses in supercritical regime are $GM_{\text{bh}} \sim H_i R_i^2$, so the bound (6) is nearly saturated. Here, we shall see that the same conclusion applies to supercritical bubbles with a sufficiently large R_i .

III. SIMULATION SETUP

In this section we consider the equations of motion as well as the initial and boundary conditions necessary for numerical simulations of a vacuum bubble embedded in an otherwise homogeneous radiation-dominated universe. We also indicate how we read the black hole mass from the simulation results and discuss some simulation issues.

A. Equations of motion and gauge conditions

The spacetime is assumed to be spherically symmetric, and the metric we use for the exterior region (outside of the bubble) is

$$ds^2 = -A^2 dt^2 + B^2 dr^2 + R^2 d\Omega^2, \quad (7)$$

where A, B and R are functions of the coordinates t and r . The radiation fluid is generally described by its energy density ρ , pressure $p = w\rho$ with $w = 1/3$, and 4-velocity $u^\mu = (u^0, u^1, 0, 0)$ with $A^2(u^0)^2 - B^2(u^1)^2 = 1$.

To fix the gauge, we choose the coordinates comoving with the fluid, in which $u^1 = 0$ and $u^0 = A^{-1}$. In this gauge, both the equations of motion and the boundary conditions take a particularly simple form. Since the fluid is confined to the bubble exterior, the normal component of the fluid velocity vanishes at the bubble wall. The tangential velocity vanishes by symmetry. It follows that the wall is comoving with the fluid; hence it remains at a fixed value of the comoving radius, $r = r_w$. With a different choice of gauge we would have to impose boundary conditions on a moving boundary, which is considerably more complicated.

Following Ref. [21] we introduce

$$U \equiv \frac{\dot{R}}{A}, \quad \Gamma \equiv \frac{R'}{B}, \quad (8)$$

where $\dot{} \equiv \partial/\partial t$ and $' \equiv \partial/\partial r$. Our goal is to solve Einstein's equations in order to find A, U, Γ, B, R and ρ . By the following transformations

$$\tilde{t} = H_i t, \quad \tilde{B} = H_i B, \quad \tilde{R} = H_i R, \quad \tilde{\rho} = \frac{\rho}{M_{\text{Pl}}^2 H_i^2}, \quad (9)$$

all variables become dimensionless. In this section we use these new variables and drop the tilde. For instance, the time at the end of inflation now becomes $t_i = (2H_i)^{-1} = 1/2$. To restore the physical value of a certain quantity, one simply needs to multiply by an appropriate conversion factor. For example, the conversion factor for mass is M_{pl}^2/H_i .

Einstein's equations then take the form

$$\frac{A'}{A} = -\frac{w}{1+w} \frac{\rho'}{\rho}, \quad (10)$$

$$\dot{U} = -A \left(4\pi w \rho R + \frac{M}{R^2} \right) + \frac{A'\Gamma}{B}, \quad (11)$$

$$\dot{\Gamma} = \frac{A'U}{B}, \quad (12)$$

$$\dot{R} = AU. \quad (13)$$

$$\dot{B} = \frac{AU'}{\Gamma}, \quad (14)$$

$$\dot{\rho} = -(1+w)\rho A \left(\frac{U'}{B\Gamma} + \frac{2U}{R} \right), \quad (15)$$

where

$$M \equiv R(1 - \Gamma^2 + U^2)/2 \quad (16)$$

is the Misner-Sharp mass parameter [22] that we shall use to characterize the mass of the central object.

Eqs. (14) and (15) can be written in an equivalent form:

$$\dot{B} = \frac{AB}{U} \left(4\pi\rho R - \frac{M}{R^2} + \frac{\Gamma'}{B} \right), \quad (17)$$

$$\dot{\rho} = -(1+w)\frac{\rho A}{U} \left(4\pi\rho R - \frac{M}{R^2} + \frac{\Gamma'}{B} + \frac{2U^2}{R} \right). \quad (18)$$

We used different equations in different situations in order to avoid a vanishing denominator. For instance, in the subcritical case, the bubble grows and then shrinks, so the value of U at the wall goes from positive to negative at the turning point. Hence we use Eqs. (14) and (15) to evolve B and ρ respectively, since $U = 0$ must not appear in the denominator. Similarly, in the supercritical case, Γ crosses zero when the wormhole throat is formed, so we use Eqs. (17) and (18).

The gauge condition $u^1 = 0$ leaves the freedom of time transformations, $t \rightarrow \bar{t}(t)$. We can fix the gauge completely by specifying $A(r, t)$ on any timelike curve. Before the bubble

is removed for reasons discussed below (Subsection IV.B), a convenient choice is to set $A(r_w, t) = 1$ at the bubble wall. Then our time coordinate t coincides with the proper time τ at the wall.

B. Boundary conditions

We first comment on the number of boundary conditions required for our problem. The following argument was suggested to us by Andrei Gruzinov.

Introducing two new variables, $C = A^3/B$ and $F = \Gamma^2 - U^2$, instead of B and Γ , the equations of motion (11)-(15) can be represented as

$$\dot{R} = \dots, \quad \dot{C} = \dots, \quad \dot{F} = \dots, \quad (19)$$

$$\dot{U} = -\frac{w}{1+w} \frac{A\Gamma}{B\rho} \rho' + \dots, \quad (20)$$

$$\dot{\rho} = -(1+w) \frac{A\rho}{B\Gamma} U' + \dots, \quad (21)$$

where "..." means terms without derivatives and we have used Eq. (10) to express A' in terms of ρ' in (20). Now, Eqs. (19) do not require boundary conditions (only initial conditions) and Eqs. (20) and (21) represent a wave with a (high-frequency) sound speed $c_s^2 = wA^2/B^2$. We thus have one propagating degree of freedom, which requires one left and one right boundary condition.

Variables outside of the shock front should be described by the unperturbed FRW solution, so the outer boundary condition is easy to impose. Before the bubble is removed, the wall serves as the inner boundary. The bubble interior is described by de Sitter space with energy density ρ_b . The boundary conditions at the wall can be obtained using Israel's junction conditions. This is done in Appendix A.⁴ As we discussed, we only need one boundary condition at $r = r_w$; we use the condition (A14):

$$A' = -AB \left(\frac{w\rho + \rho_b}{\sigma} + \frac{2\Gamma}{R} + 6\pi\sigma \right). \quad (22)$$

We also set $A = 1$ on the inner boundary at all times, even after the bubble wall is removed.

⁴ The equation of motion of the wall is also derived in Appendix A, but we did not use it in our simulations.

C. Initial conditions

We assume an idealized initial state where inflation ends instantaneously at $t = t_i$ and false vacuum energy immediately turns into radiation of uniform energy density

$$\rho_i = \frac{3}{32\pi t_i^2} = \frac{3}{8\pi}. \quad (23)$$

Since the lapse function $A = 1$ at $r = r_w$, it follows from Eq. (10) that $A(r, t_i) = 1$ in the entire region outside of the bubble. One might expect that at $t = t_i$ this whole region is described by the FRW solution. Then, with a suitable normalization of r , we would have $B(r, t_i) = 1$, $R(r, t_i) = r$, $U(r, t_i) = r/2t_i$, and $\Gamma(r, t_i) = 1$. However, these values cannot be imposed as initial conditions in the entire region $r > r_w$.

At the initial moment, the bubble wall moving with a large Lorentz factor comes into contact with the radiation fluid that surrounds it. On the other hand, we are working in a gauge where the radiation is comoving with the wall at $r = r_w$. Clearly, this condition cannot be satisfied if the FRW solution outside the bubble is unperturbed. We deal with this problem by modifying the FRW solution in a thin layer around the bubble.

The Misner-Sharp mass of the bubble at t_i is $M(r_w, t_i) = H_i^2 R_i^3/2 = r_w^3/2$, where we have assumed that $R_i = r_w$. On the other hand, $M(r_w, t_i)$ is also given by Eq. (1) with $R_w = R_i$. Then by the definition of U and M , the initial value of Γ at the wall is given by

$$\Gamma(r_w, t_i) = \left(\frac{1 - H_b^2}{4H_\sigma} - H_\sigma \right) r_w. \quad (24)$$

To smooth out the discontinuity between this and the FRW value of $\Gamma = 1$, we use the following function for the initial profile of Γ ,

$$\Gamma(r, t_i) = [1 - \Gamma(r_w, t_i)] \tanh\left(\frac{r - r_w}{\delta}\right) + \Gamma(r_w, t_i), \quad (25)$$

where δ characterizes the thickness of the layer that connects the wall and the FRW universe.

To fix the remaining initial conditions, we assume the spatial metric $ds^2 = B^2(dr^2 + r^2 d\Omega^2)$. Then $R(r, t_i) = B(r, t_i)r$ and it follows from the definition of Γ that

$$\frac{R'r}{R} = \Gamma. \quad (26)$$

$R(r, t_i)$ can now be found by numerically integrating Eq. (26). To illustrate the deviation of our initial state from FRW, we plot the functions $B(r, t_i)$ and $\dot{R}(r, t_i)/R(r, t_i)$ in Fig. 4. (Both of these functions are equal to 1 in an FRW universe.)

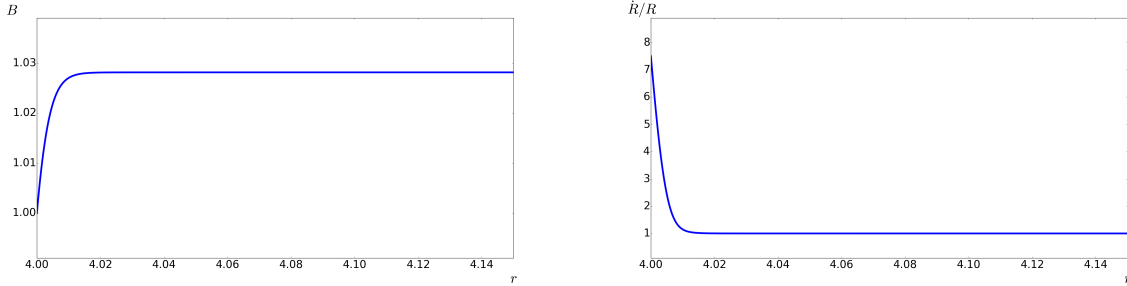


FIG. 4: The initial profiles of B and \dot{R}/R for a bubble with $R_i = 4$.

The Misner-Sharp mass within a radius r at t_i can be found from the relation [23] $M' = 4\pi\rho R^2 R'$, which gives $M(r, t_i) = R^3(r, t_i)/2$. Then by the definition of M , the initial profile of U is

$$U(r, t_i) = \sqrt{R^2 + \Gamma^2 - 1}. \quad (27)$$

It can be shown [16] that in our gauge the initial value of U at the wall is related to the initial Lorentz factor of the wall γ (relative to an FRW observer) by

$$U(r_w, t_i) = R_i\gamma + \sqrt{\gamma^2 - 1}. \quad (28)$$

In our simulations, we used H_b and γ as free parameters. The value of H_σ can be determined from Eqs. (1), (8) and (28).

A profile of $U(r, t_i)$ with a finite δ means that the fluid already acquired some kinetic energy at t_i in a layer of width δ . It is shown in Ref. [16] that the wall loses most of its kinetic energy and comes to rest with respect to the radiation fluid within a time $\Delta t \sim H_\sigma^2/H_i^3$ (a more accurate calculation gives $\Delta t \sim 100H_\sigma^2/H_i^3$). This suggests that δ should be chosen so that $\delta \lesssim \Delta t$. Indeed, we have verified that reducing δ below this value does not have a significant impact on the black hole mass.

D. Expansions and horizons

We determine the formation of a black hole by checking if an apparent horizon bounding a trapped region is formed. Let Θ_{out} and Θ_{in} be the expansions of outgoing and ingoing radial null geodesics respectively; then a surface is trapped if $\Theta_{\text{out}}, \Theta_{\text{in}} < 0$, and anti-trapped if $\Theta_{\text{out}}, \Theta_{\text{in}} > 0$. In our coordinate system [25],

$$\Theta_{\text{out}} \propto \frac{U + \Gamma}{R}, \quad \Theta_{\text{in}} \propto \frac{U - \Gamma}{R}. \quad (29)$$

The apparent horizon of a black hole is foliated by marginal spheres with $\Theta_{\text{out}} = 0$ and $\Theta_{\text{in}} < 0$. We also define the white hole (apparent) horizon and cosmological (apparent) horizon to be hypersurfaces foliated by marginal spheres with $\Theta_{\text{in}} = 0$ and $\Theta_{\text{out}} > 0$. A spherical surface is anti-trapped within the white hole horizon, and is normal (with $\Theta_{\text{in}} > 0$ and $\Theta_{\text{out}} > 0$) if it lies between the white (or black hole) and the cosmological horizon. The cosmological horizon and the Hubble radius coincide in a flat FRW universe.

E. Simulation issues

We use finite-difference method and Runge-Kutta integration to solve the PDEs.

Special attention is needed on the shock wave. The shock formed by the interaction of the fast-moving wall and the radiation may lead to numerical instability. A standard and convenient trick to handle this is to introduce artificial viscosity [27] in order to smooth out the discontinuity. Following [26], we add an extra term to w ,

$$w \rightarrow \frac{1}{3} + \beta \Delta r^2 \left(\frac{U'}{R'} + \frac{2U}{R} - \left| \frac{U'}{R'} + \frac{2U}{R} \right| \right) \left(\frac{U'}{R'} - \frac{U}{R} \right), \quad (30)$$

where β is an adjustable coefficient that controls the viscosity strength, and Δr is the grid size. When needed, we replace U'/R' by

$$\frac{U'}{R'} \rightarrow U^{-1} \left(4\pi\rho R - \frac{M}{R^2} + \frac{\Gamma'}{B} \right) \quad (31)$$

to avoid $R' = 0$ in the denominator in Eq. (30).

Additionally, in order to improve the efficiency of the code, we use an adaptive non-uniform mesh. At the beginning of the simulation, a sufficiently high resolution is used until a shock wave is formed. Then we reduce the mesh density in regions far away from the shock. We keep track of the shock and make sure there is a sufficient number of grid points there.

Another issue is related to the early evolution of the bubble wall. A very large initial Lorentz factor γ tends to break down the code before any desirable results are obtained. Throughout the simulations we used $\gamma \lesssim 10$. This leads to a constraint on H_σ . The initial Lorentz factor can be estimated as [16] $\gamma \sim H_\sigma^{-1}$. Using this and Eqs. (4) and (5), it can be shown that the radii of subcritical bubbles must satisfy $R_i \lesssim \gamma$. On the other hand, we are mostly interested in bubbles of initial radius greater than the horizon, $R_i \gtrsim 1$. This gives

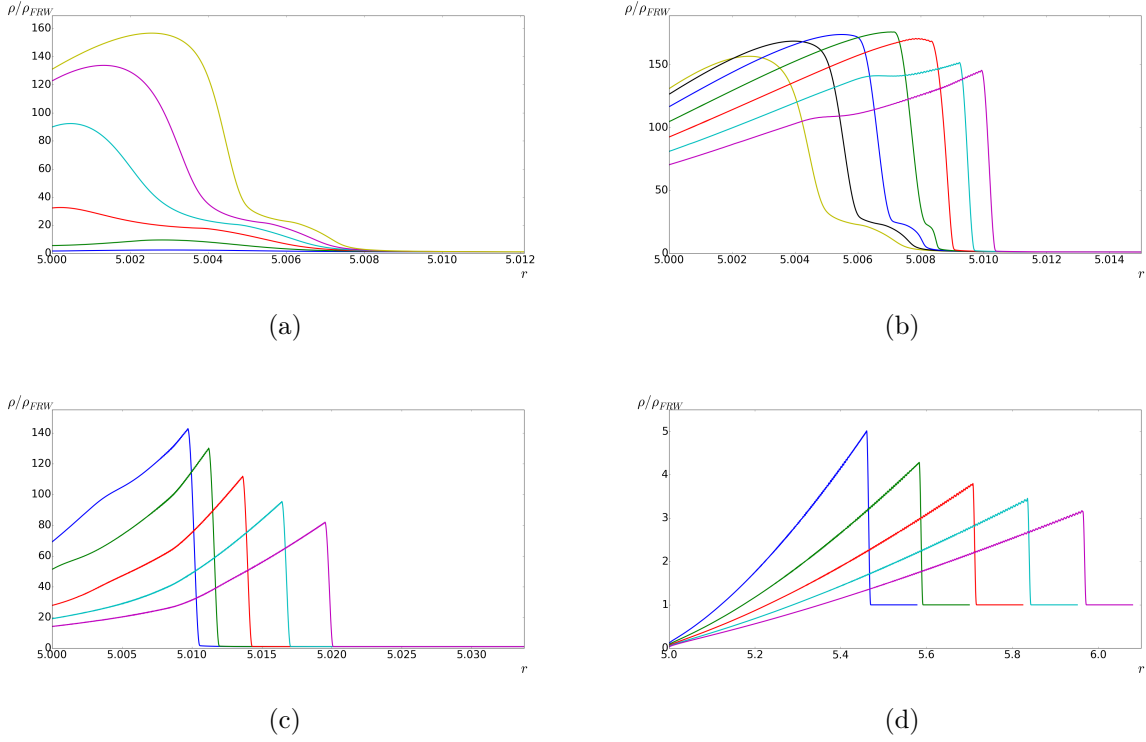


FIG. 5: The radiation energy density ρ as a function of the comoving radius r at different moments of time outside of a subcritical bubble with $H_b = 0.05H_i$, $H_\sigma \approx 0.03H_i$, and $R_i = 5H_i^{-1}$. For all moments, ρ has been rescaled so that the FRW density is 1. (a), (b) and (c) are taken at FRW times t when $t - t_i \ll t_i$, while (d) is at t when $t - t_i \sim t_i$. (a) An overdense layer is formed next to the wall as it hits the fluid. (b) A shock wave forms and propagates outwards, while the density at the wall begins to decrease. (c) The shock continues to propagate with the density contrast across the shock rapidly decreasing. (d) ρ right outside the wall becomes much smaller than the FRW density, as if the bubble is surrounded by an empty layer, much like in the case of a dust background.

a rather limited range of values for R_i . For supercritical bubbles, we are free to use a large value for R_i , but are restricted by the simulation runtime.

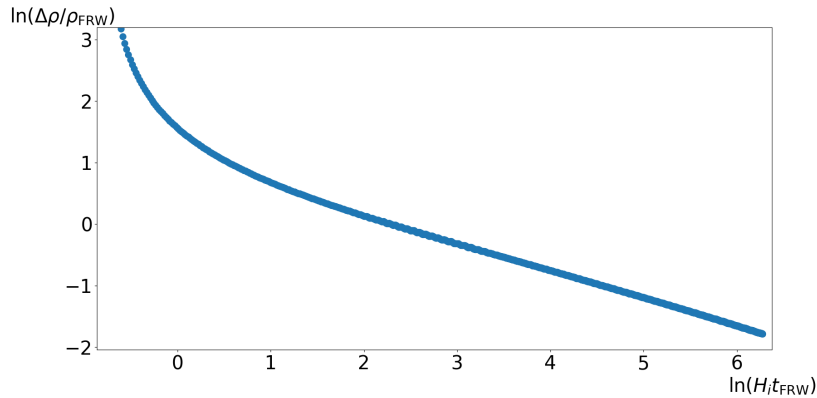


FIG. 6: The density contrast across the shock δ_s as a function of time for the subcritical bubble in Fig 5. As the shock propagates outwards, it approaches the speed of sound and satisfies $\delta_s(t) \propto t^\epsilon$, where $\epsilon \approx -1/2$. In the example shown here $\epsilon \approx -0.46$.

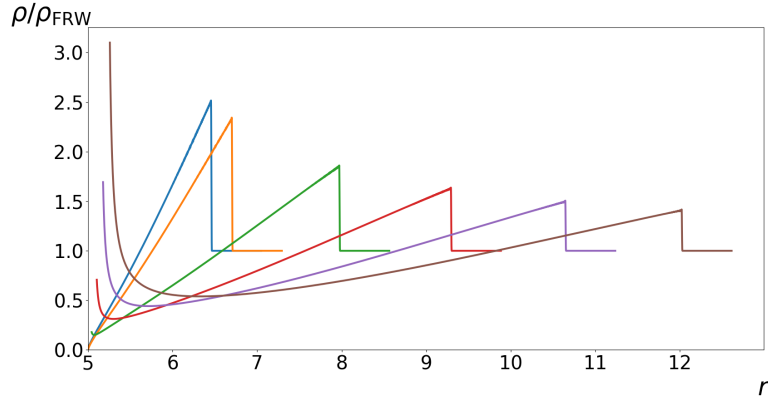
IV. SIMULATION RESULTS

A. Shock propagation

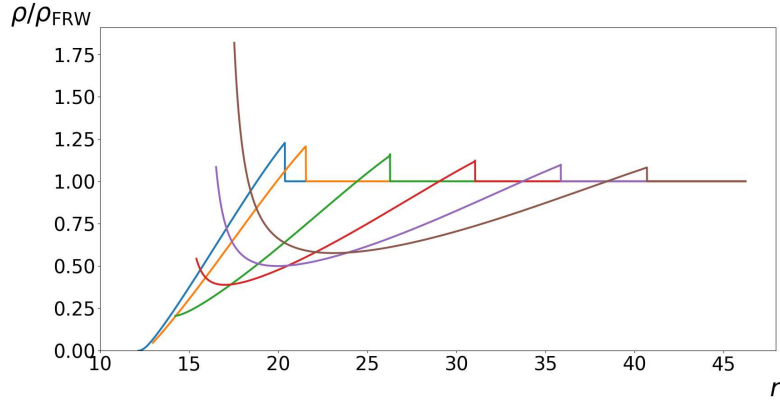
The formation and propagation of the shock wave produced by the bubble are illustrated in Fig. 5. The figure shows the radiation density profile at successive moments of time. As the bubble wall hits the ambient radiation, a thin overdense layer is formed right outside the wall. In this example, the density in the layer exceeds that in the FRW region by more than 100 times. The overdense layer spreads and develops a sharp shock front, which then propagates outwards. Meanwhile, the radiation density next to the wall rapidly drops, and in less than a Hubble time becomes much smaller than that in the FRW region.

The density contrast across the shock $\delta_s \equiv \Delta\rho/\rho_{\text{FRW}}$, where $\Delta\rho \equiv \rho_{\text{shock}} - \rho_{\text{FRW}}$, is very large immediately after the wall hits the ambient radiation, but rapidly drops and becomes $\mathcal{O}(1)$ in about a Hubble time. Fig. 6 shows the subsequent evolution of δ_s , which can be approximated as $\delta_s(t) \propto t^{-1/2}$.

As the shock propagates outwards, the empty layer created by the bubble impact is gradually filled with radiation. In Fig. 7 we show the radiation density profile at several moments right before and after black hole formation, both for a subcritical and a supercritical bubble. In both cases, in a few Hubble times after the black hole is formed, it is surrounded by a nearly uniform radiation background.



(a) $H_b = 0.05H_i$, $H_\sigma \approx 0.03H_i$, and $R_i = 5H_i^{-1}$



(b) $H_b = 0.75H_i$, $H_\sigma \approx 0.02H_i$, and $R_i = 10H_i^{-1}$

FIG. 7: The radiation energy density ρ as a function of the comoving radius r for a subcritical (upper panel) and a supercritical (lower panel) bubble at different moments before and after black hole formation. In both plots, the first (blue) and the second (orange) density profiles respectively correspond to moments right before and after the black hole is formed. After black hole formation, the shock continues to diminish and the density deficit in the black hole vicinity is gradually filled with radiation. We cut off the black hole region at the apparent horizon in order to avoid simulation breakdown. In the subcritical case, the apparent horizon arises at the wall; while in the supercritical case, it appears at the wormhole throat. At the first moment (blue) in the second plot, we have already removed the wall and a surrounding layer to avoid simulation breakdown due to the inflating wall.

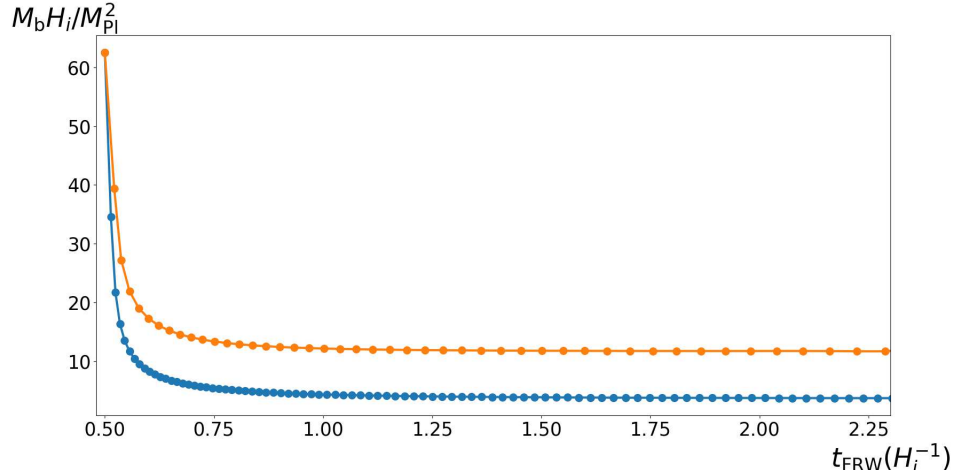


FIG. 8: The early evolution of the Misner-Sharp mass for a subcritical (blue; $H_\sigma \approx 0.03H_i$, $H_b = 0.05H_i$ and $R_i = 5H_i^{-1}$) and a supercritical (orange; $H_\sigma \approx 0.05H_i$, $H_b = 0.25H_i$ and $R_i = 5H_i^{-1}$) bubble. In both cases, the bubble loses most of its energy within a time scale much smaller than the Hubble time H_i^{-1} . The mass continues to change due to the radiation pressure, but in about a Hubble time this effect becomes negligible, and the Misner-Sharp mass approaches the conserved mass parameter \mathcal{M}_b . In the subcritical case the initial black hole mass is $M_{\text{bh}} \sim \mathcal{M}_b$, while for supercritical bubbles M_{bh} is not simply related to \mathcal{M}_b .

B. Black hole mass

1. Subcritical bubble

The Misner-Sharp mass of the bubble decreases dramatically within a time scale $\Delta t \ll t_i$ due to momentum transfer to radiation. At later times, the mass continues to change due to the radiation pressure, but it approaches a constant after about one Hubble time (Fig. 8). In the subcritical case, the bubble radius R_w reaches a maximum and then decreases. An apparent horizon is formed when $\Theta_{\text{out}} = 0$ at the wall. We regard this as a signal of black hole formation. The black hole mass can be estimated as the Misner-Sharp mass at the apparent horizon.

The black hole masses obtained from the simulations are compared with the analytic estimate (4) in Table. I. We see that Eq. (4) gives a good estimate within a factor of 2. As expected, in most examples the actual black hole mass is lower than estimated, because of

Parameters(H_i)	$R_i(H_i^{-1})$	$M_{\text{est}}(M_{\text{Pl}}^2 H_i^{-1})$	$M_{\text{bh}}(M_{\text{Pl}}^2 H_i^{-1})$
$H_b = 0.05, H_\sigma \approx 0.03$	2	0.5	0.3
	3	1.7	1.0
	4	3.9	2.1
	5	7.6	3.7
$H_b = 0.25, H_\sigma \approx 0.03$	2	0.8	0.7
$H_b = 0.5, H_\sigma \approx 0.01$	1.8	0.8	0.9
$H_b = 0.75, H_\sigma \approx 0.02$	1	0.3	0.3

TABLE I: Black hole masses for six subcritical bubbles. M_{est} is the estimate given by Eq. (4), and M_{bh} is the simulation result.

the radiation pressure during the expansion phase of the bubble. In some examples, however, the actual mass is slightly higher. This is because the expansion phase in these cases was very short.

At later times, the black hole mass grows by accretion of radiation, but the resulting mass increase is no more than by a factor of 2 [17].

2. Supercritical bubble

In the supercritical case, a wormhole develops outside of the bubble wall, and the bubble starts to inflate. In Fig. 9 we show the area radius R as a function of the comoving radius r at several successive moments of time. We see that $R(r)$ develops a minimum outside of the wall, signaling the formation of a wormhole. Since the bubble is rapidly expanding, the radius $R(r)$ grows sharply towards the wall.

In order to simulate the evolution of the region near the bubble wall, high resolution is needed. However, since the bubble grows supersonically away from the exterior region and thus gets detached from the fluid, we cut off the wall as well as a layer immediately outside, so as to prevent $R(r)$ from changing steeply near the inner boundary and avoid simulation breakdown. This excision does not affect the evolution of the exterior region.

The black hole formation is signaled by the horizon bifurcation point, where $\Theta_{\text{out}} = \Theta_{\text{in}} = 0$. (This is the point at the intersection of the two apparent horizon lines in the conformal

diagram of Fig. 3.) At this point two black holes of equal mass are formed, one for the observer in the baby universe and the other in the exterior FRW universe.

The two black holes start with identical masses, but the masses can grow later by accretion and do not have to remain equal. The mass accretion on the exterior black hole has been studied in Ref. [17] in the domain wall scenario, with the conclusion that it increases the black hole mass by approximately a factor of 2. For a large supercritical bubble, the perturbation caused by the shock should mostly dissipate by the time of black hole formation, and we expect that the accretion process will be very similar to the domain wall case, with similar result.

In Fig. 10 we plotted the ratio $M_{\text{bh}}/M_{\text{Pl}}^2 H_i R_i^2$ for a range of values of R_i . We see that as R_i increases, the ratio approaches a constant $\mathcal{O}(1)$,

$$M_{\text{bh}} \sim M_{\text{Pl}}^2 H_i R_i^2. \quad (32)$$

Thus, for large values of R_i the bound (6) is nearly saturated, as in the domain wall scenario.

The data points with $R_i < H_i^{-1}$ correspond to subcritical regime, where we expect $M_{\text{bh}} \sim \kappa M_{\text{Pl}}^2 R_i^3$ with κ defined from Eq.(4),

$$\kappa \equiv \frac{1}{2} H_b^2 + 2H_\sigma \left(\sqrt{H_i^2 - H_b^2} - H_\sigma \right). \quad (33)$$

For the parameter values in Fig. 10, $\kappa \sim 0.3H_i^2$. This estimate is in agreement with the simulation results.

In conclusion, we can roughly approximate our results by setting

$$M_{\text{bh}} \sim M_{\text{Pl}}^2 \begin{cases} \kappa R_i^3 & M < M_* \\ H_i R_i^2 & M > M_*, \end{cases} \quad (34)$$

where the transition mass

$$M_* \sim \frac{M_{\text{Pl}}^2 H_i^3}{\kappa^2} \quad (35)$$

corresponds to $R_* \sim H_i/\kappa$.

Parameters used in Fig. 10 give $R_* \sim 3H_i^{-1}$. In this case M_* is not much different from M_{cr} , but for other parameter values these two masses can be rather different. For example, if the first term in κ dominates, we have $M_*/M_{\text{cr}} \sim (H_i/H_b)^3$, which can be large for $H_b \ll H_i$. Restricted by the capability of our simulation, we did not further explore the transition regime $M_{\text{cr}} \lesssim M_{\text{bh}} < M_*$.

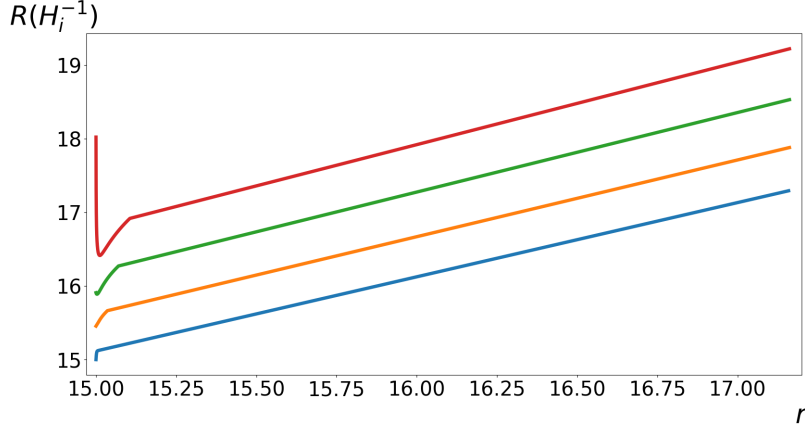


FIG. 9: The area radius $R(r)$ at different times for a supercritical bubble with $H_b = 0.75H_i$, $H_\sigma \approx 0.02H_i$ and $R_i = 15H_i^{-1}$. The bottom blue curve is the initial profile of R . In the unperturbed FRW region, $R \propto r$. A local minimum develops with time, indicating the formation of a wormhole throat. The wall inflates away exponentially afterwards, so R grows sharply near the wall.

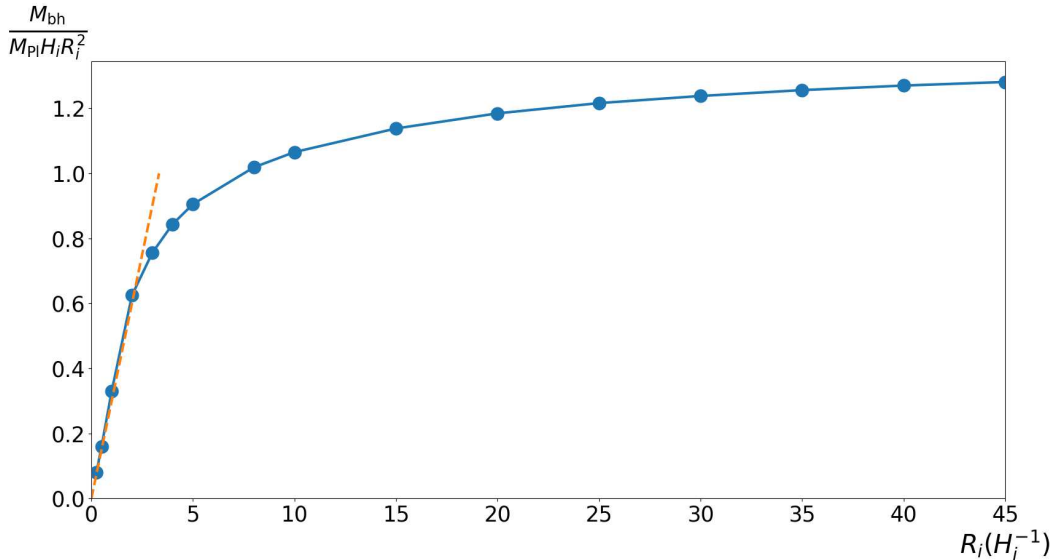


FIG. 10: Black hole mass as a function of R_i . Blue dots are $M_{\text{bh}}/M_{\text{Pl}}^2 H_i R_i^2$ for bubbles with $H_i R_i = 0.25, 0.5, 1, 2, 3, 4, 5, 8, 10, 15, 20, 25, 30, 35, 40$ and 45 . In all cases, $H_\sigma \approx 0.02H_i$ and $H_b = 0.75H_i$. For these parameter values, the critical radius is $R_{\text{cr}} \sim 1.3H_i^{-1}$ and the transition radius $R_* \sim 3H_i^{-1}$. The orange dashed line shows our estimate for subcritical cases. We can see that the estimate works well even for the supercritical case with $R_i = 2H_i^{-1}$.

V. BLACK HOLE MASS SPECTRUM

In earlier sections we have shown how a black hole could be formed by a vacuum bubble after inflation and how its mass is related to the initial bubble radius R_i . During inflation the universe expands by a huge factor, so the bubble radii spread over a large range of scales. In this section we calculate the distribution of R_i and find the resulting PBH mass spectrum. The calculation follows closely that in Ref. [16].

A. Size distribution of bubbles

To simplify the notation, in this subsection we use R to denote the bubble radius during inflation.

The background spacetime during inflation can be described by a flat de Sitter metric,

$$ds^2 = -dt^2 + a^2(t)d\mathbf{x}^2 \quad (36)$$

with $a(t) = H_i^{-1} \exp(H_i t)$. Let t_n be the bubble nucleation time. For simplicity, we assume that the bubble nucleates with a negligible radius compared to H_i^{-1} ; then the bubble worldsheet is well approximated by the future light cone of the nucleation point,

$$R(t) \approx H_i^{-1} [e^{H_i(t-t_n)} - 1]. \quad (37)$$

The number of bubbles that materialize in a coordinate interval $d^3\mathbf{x}$ and time interval dt_n is

$$dN = \lambda H_i^4 e^{3H_i t_n} d^3\mathbf{x} dt_n, \quad (38)$$

where λ is the bubble nucleation rate per Hubble spacetime volume H_i^{-4} .

The number density of bubbles having radius in the interval $(R, R + dR)$ at time t is

$$dn(t) \equiv \frac{dN}{dV} = \lambda \frac{dR}{(R + H_i^{-1})^4}, \quad (39)$$

where

$$dV \equiv e^{3H_i t} d^3\mathbf{x} \quad (40)$$

is the physical volume element at t .

The distribution (39) applies in the range $R \lesssim H_i^{-1} e^{\mathcal{N}}$, where \mathcal{N} is the number of inflationary e-folding. During inflation, the form of the distribution does not change with time, except the upper cutoff increases, reaching its maximum at the end of inflation.

B. Black hole mass distribution

To simplify the notation, in this and the next subsection we replace M_{bh} by M .

By Eq. (39), the number density of bubbles within the radius range $(R_i, R_i + dR_i)$ at the end of inflation is

$$dn(t_i) = \lambda \frac{dR_i}{(R_i + H_i^{-1})^4}. \quad (41)$$

After t_i the bubble population is diluted by cosmic expansion, i.e.

$$dn(t) = dn(t_i) \left[\frac{a(t_i)}{a(t)} \right]^3, \quad (42)$$

where $a(t) \propto t^{1/2}$ is the scale factor and we assume that the black holes are formed during the radiation era.

We use the standard definition of the mass function

$$f(M) = \frac{M^2}{\rho_{\text{CDM}}(t)} \frac{dn(t)}{dM}, \quad (43)$$

where $\rho_{\text{CDM}}(t)$ is the mass density of cold dark matter (CDM). Here $M^2 dn/dM$ can be interpreted as the mass density of black holes in the mass range $\Delta M \sim M$. Since the black hole density and ρ_{CDM} are diluted by the cosmic expansion in the same way, $f(M)$ remains constant in time. The total fraction of CDM in PBHs can be expressed as

$$f_{\text{PBH}} \equiv \frac{\rho_{\text{PBH}}(t)}{\rho_{\text{CDM}}(t)} = \int \frac{dM}{M} f(M), \quad (44)$$

where $\rho_{\text{PBH}}(t)$ is the PBH mass density.

During the radiation era ($t < t_{\text{eq}}$), the dark matter density is of the order

$$\rho_{\text{CDM}}(t) \sim \frac{1}{BGt^2} \left(\frac{t}{t_{\text{eq}}} \right)^{1/2} \sim \frac{M_{\text{Pl}}^3}{Bt^{3/2} \mathcal{M}_{\text{eq}}^{1/2}}, \quad (45)$$

where $B \sim 10$ is a constant and $\mathcal{M}_{\text{eq}} \sim t_{\text{eq}}/G \sim 10^{17} M_{\odot}$ is the dark matter mass within a Hubble radius at t_{eq} .

To find the mass function for our model, we use the simple ansatz (34) for $M(R_i)$. For bubbles with $R_i \gg H_i^{-1}$, we can neglect H_i^{-1} in Eq. (41). Then, for black holes with $M > M_*$ we have

$$\frac{dn(t)}{dM} \sim \frac{\lambda M_{\text{Pl}}^3}{M^{5/2} t^{3/2}}. \quad (46)$$

and

$$f(M) \sim B\lambda \left(\frac{\mathcal{M}_{\text{eq}}}{M} \right)^{1/2}. \quad (47)$$

For $M < M_*$, we use $M \propto R_i^3$, which gives $dn/dM \propto M^{-2}$ and $f(M) = \text{const.}$ Hence the resulting mass function has the form

$$f(M) \sim B\lambda \mathcal{M}_{\text{eq}}^{1/2} \begin{cases} M_*^{-1/2} & M < M_* \\ M^{-1/2} & M > M_* \end{cases}, \quad (48)$$

The distribution (48) becomes inaccurate for black holes of mass

$$M \lesssim \kappa M_{\text{Pl}}^2 H_i^{-3} \equiv M_H, \quad (49)$$

formed by bubbles with $R_i \lesssim H_i^{-1}$ that nucleated during the last e-fold of inflation. For $R_i \ll H_i^{-1}$, Eq. (1) gives

$$GM \sim \left(\frac{1}{2} H_b^2 - 2H_\sigma^2 \right) R_i^3 + 2H_\sigma R_i^2. \quad (50)$$

If the first term dominates, $f(M) \propto M^{4/3}$; if the second term dominates, then $f(M) \propto M^{3/2}$. In either case, the mass function decreases relatively fast at $M < M_H$, and thus M_H plays the role of a lower cutoff for the distribution (48).

Another cutoff mechanism is due to shape fluctuations of the bubbles.⁵ At the time of nucleation, bubbles are not perfectly spherical, because of quantum fluctuations. The amplitude of these fluctuations and their subsequent evolution have been discussed in Refs. [29, 30]. When a subcritical bubble collapses, the shape fluctuations grow and may become large before the bubble shrinks to its Schwarzschild radius. The bubble will then fragment into smaller pieces, which will in turn disintegrate into relativistic particles, so no black hole will be formed. We show in Appendix B that the corresponding lower bound on the black hole mass is

$$M_{\text{bh}} \gtrsim \rho_b \left(\frac{\rho_i M_{\text{Pl}}}{\rho_b \sigma} \right)^{3/2} \equiv M_F. \quad (51)$$

Some black holes with $M_{\text{bh}} < M_F$ may still be formed from bubbles with atypically small shape fluctuations. We have not explored the mass distribution in this regime.

⁵ We are grateful to Jaume Garriga for emphasizing this to us.

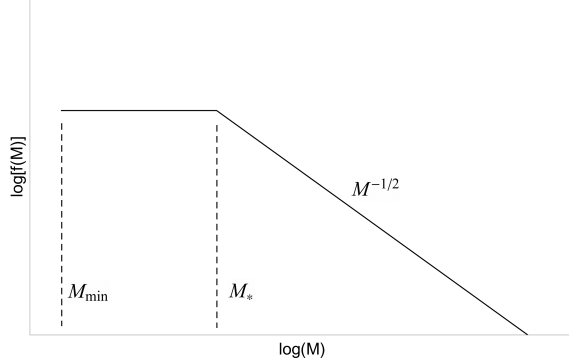


FIG. 11: A general form of our mass function, Eq. (48). The mass function at $M < M_{\min}$ rapidly declines towards zero. Its shape depends on the cutoff mechanism and is not shown here.

The shape fluctuations have no effect on the evolution of supercritical bubbles, thus the lower bound cannot be larger than M_{cr} . Therefore, the mass function (48) is effectively cut off at

$$M_{\min} \sim \begin{cases} \max\{M_H, M_F\}, & M_F < M_{\text{cr}} \\ M_{\text{cr}}, & M_F > M_{\text{cr}} \end{cases}. \quad (52)$$

Depending on the microphysical energy scales ρ_i and ρ_b , the mass parameters M_* and M_{\min} can take a very wide range of values. For example, with ρ_i and ρ_b varying between the electroweak and grand unification scale, M_* can be as small as a few grams and can be larger than the mass of the entire observable universe, while M_{\min} is restricted to $M_{\min} \lesssim 10^{-4} M_{\odot}$. On the other hand, if the scale of ρ_b is less than the electroweak scale, M_{\min} can be much larger. Here we shall treat M_* and M_{\min} as free parameters. A general form of the mass function is illustrated in Fig. 11.

By Eq. (44), the total mass fraction of dark matter in PBH is given by

$$f_{\text{PBH}} \sim B\lambda \left(\frac{\mathcal{M}_{\text{eq}}}{M_*} \right)^{1/2} \left[\ln \left(\frac{M_*}{M_{\min}} \right) + 1 \right]. \quad (53)$$

VI. OBSERVATIONAL PROPERTIES AND CONSTRAINTS

Apart from the distinctive mass spectrum, black holes produced by our mechanism have other interesting properties.

At the time of formation, these black holes are non-rotating. They may acquire some angular momentum by accretion of matter at later times, but much of the accretion occurs

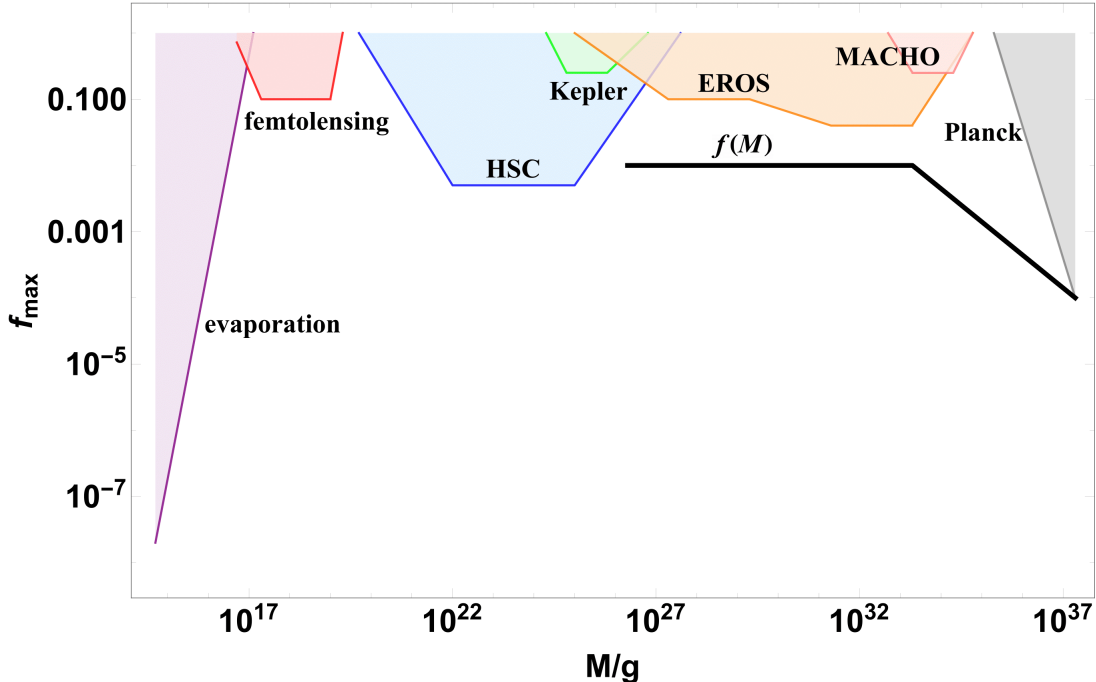


FIG. 12: A sketch of constraints from different observations on the fraction of dark matter in PBHs as a function of the PBH mass for a monochromatic mass distribution. More detail can be found in e.g. Ref. [34, 36] and references therein. As an illustration, we also show the PBH distribution for our model with $\lambda \sim 10^{-12}$, $M_* = M_\odot$ and $M_{\min} = 10^{-7} M_\odot$, which is marginally consistent with the constraints.

in the radiation era, within a few Hubble times after formation, and is likely to be nearly spherically symmetric. Hence we expect this population of black holes to be very slowly rotating. It is interesting to note that LIGO observations suggest low spins for the merging black holes [31].

Scenarios of PBH formation from large primordial density fluctuations predict a background of stochastic gravitational waves, imposing significant constraints on this PBH formation mechanisms. Another stringent constraint comes from the observational bounds on the μ -distortion of the CMB spectrum. (For a discussion of these constraints, see, e.g. [32, 33] and references therein). Our model does not require large initial fluctuations and is not subject to these constraints.

We now turn to observational constraints on our PBH formation model. Constraints on PBHs in different mass ranges have been extensively studied in the literature; see, e.g., [34] for an up to date review. We have indicated the current constraints in Fig. 12. A very

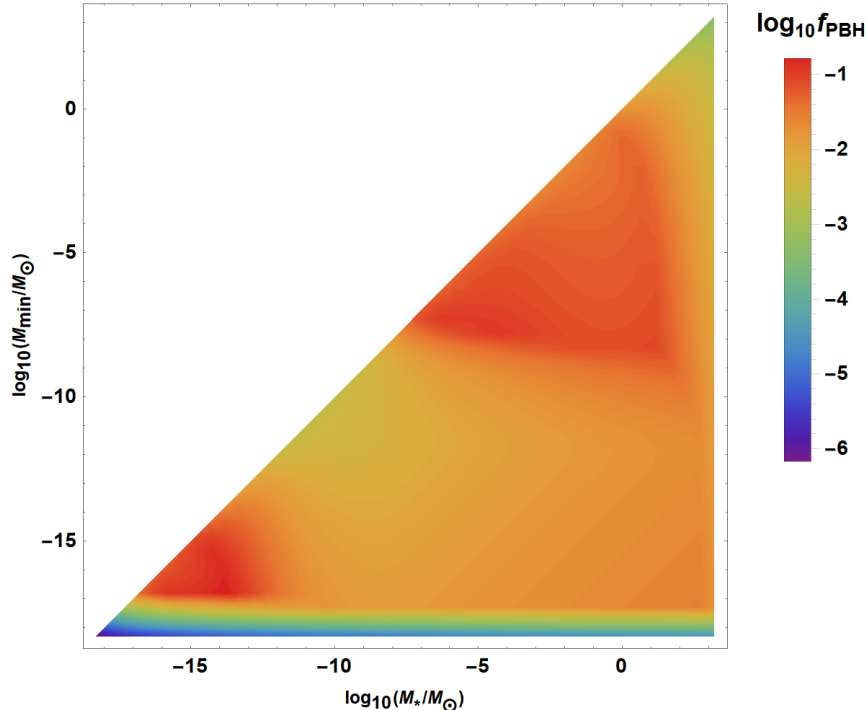


FIG. 13: Observational upper bound on the fraction of dark matter in PBHs for different values of the model parameters M_* and M_{\min} . It can be seen that in our model PBHs can constitute no more than $\sim 10\%$ of the dark matter.

stringent constraint on PBHs with $M \sim M_{\text{evap}} \sim 10^{15}$ g comes from Hawking evaporation. For our mass function (48), a substantial mass fraction in PBHs can be obtained only if the cutoff mass is $M_{\min} > M_{\text{evap}}$.

As discussed in Refs. [34–36], applying the constraints to models like ours, with a broad mass distribution of PBH, requires a special analysis. For example, observations like EROS, MACHO and HSC provide bounds $f_{\text{max}}(M)$ over several orders of magnitude. For a "monochromatic" mass distribution, these bounds simply imply $f(M) < f_{\text{max}}$, but for an extended mass distribution they give a somewhat stronger constraint [36]

$$\int_{M_1}^{M_2} \frac{dM}{M} \frac{f(M)}{f_{\text{max}}} < 1, \quad (54)$$

where $M_1 < M < M_2$ is the range of masses covered by a particular observation. The resulting upper bound on the fraction of dark matter in PBHs (f_{PBH}) for different values of the model parameters M_* and M_{\min} is shown in Fig. 13. It follows from the figure that PBHs in our model can at best constitute of order 10% of the dark matter.

Recent interest in PBHs is largely inspired by LIGO observations of gravitational waves

emitted by inspiraling black holes with $M \sim 10 - 30 M_\odot$. It has been suggested in [37] that PBHs in this range of masses with $f(M) \sim 10^{-3}$ could have a sufficient merger rate to account for LIGO results.⁶ This PBH density can in fact be achieved in our scenario. One example with $M_* \sim M_\odot$ and $\lambda \sim 10^{-12}$ is shown in Fig. 12.

Another interesting possibility is that PBHs could serve as seeds for supermassive black holes (SMBH) observed at the galactic centers. The mass of such primordial seeds should be $M \gtrsim 10^3 M_\odot$ [41], and could be significantly higher. Their number density at present should be comparable to the density of large galaxies, $n_G \sim 0.1 \text{ Mpc}^{-3}$. The relevant question for our scenario is then: What is the largest PBH we can expect to find in a galaxy?

The number density of PBHs of mass $\sim M$ is approximately given by

$$n(M) \sim \rho_{\text{CDM}} f(M) / M. \quad (55)$$

For $M > M_*$ the mass function depends only on the nucleation rate λ , and requiring that $n(M) \sim n_G$ we find $M \sim 10^{14} \lambda^{2/3} M_\odot$. For $\lambda \sim 10^{-12}$ (which is the upper bound of λ), this is $\sim 10^6 M_\odot$, which would certainly be sufficient to seed SMBH.

We thus see that for some values of the parameters black holes produced by high-energy bubbles can have interesting astrophysical implications. In particular, they could seed SMBH and could account for LIGO observations.

VII. CONCLUSIONS AND DISCUSSION

In this paper we used numerical simulations to study primordial black holes formed by vacuum bubbles created during inflation. At the end of inflation the bubbles have a scale-invariant size distribution, and we found in Eq. (34) how the black hole mass is related to the bubble radius. Bubbles smaller than certain critical size collapse to a Schwarzschild singularity; their mass has been estimated analytically in Ref. [16]. Supercritical bubbles, on the other hand, inflate in a baby universe, and [16] only found an upper bound on the black hole mass in this case. Here we confirmed the estimate of [16] for subcritical bubbles and showed that supercritical bubbles nearly saturate the upper bound on the black hole mass.

⁶ Ref. [38] suggested that a significantly higher PBH density was required, $f(M \sim 10 M_\odot) \sim 0.1 - 1$. But recent detailed analysis in [39] supports the conclusions of [37].

Black holes in this model have a very wide mass distribution, Eq.(48), stretching over many orders of magnitude. This distribution has a characteristic mass M_* and has a distinctly different form at $M_{\text{bh}} > M_*$ and $M_{\text{bh}} < M_*$. There is also a cutoff mass M_{min} below which $f(M_{\text{bh}})$ rapidly declines towards zero. Depending on the microphysics parameters, the characteristic mass M_* can take a wide range of values, from less than a kilogram to much greater than M_{\odot} .

The distribution at $M_{\text{bh}} > M_*$ has the same form, $f(M_{\text{bh}}) \propto M_{\text{bh}}^{-1/2}$, as that predicted in models where black holes are formed by scale-invariant density fluctuations in a radiation-dominated universe [28]. Black holes in this scenario are formed on the horizon scale, as in the supercritical regime of our model, so the coincidence of the mass functions is not surprising. We note, however, that the overdensity required for a horizon-size region of radiation to collapse is $\delta\rho/\rho \sim 1$, and in order to form a substantial number of black holes the rms density fluctuations should be $(\delta\rho/\rho)_{\text{rms}} \gtrsim 0.1$, much larger than that indicated by CMB and large-scale structure observations. For this reason, models predicting appreciable black hole formation from density fluctuations assume that the primordial fluctuation spectrum has an enhanced amplitude at relatively small scales (e.g., [32, 33]).

A mass distribution $\propto M_{\text{bh}}^{-1/2}$ is also predicted in models closely related to ours, where PBH are formed by spherical domain walls [16, 17] or circular loops of cosmic string [14] formed during inflation. The domain wall model also has a characteristic mass M_* above which black holes contain inflating baby universes. In the string model, the mass spectrum extends to very small masses and the black hole density is severely constrained by the Hawking radiation bound.

Considering the constraints from different observations, we found an upper bound on the fraction of dark matter in PBHs in our model, shown in Fig. 13. PBHs here can constitute no more than about 10% of the dark matter. Furthermore, we found that the fraction of dark matter in PBHs with mass $M_{\text{bh}} \sim 10 - 30 M_{\odot}$ is $\lesssim 10^{-2}$, which implies that the black holes detected in LIGO events could be the PBHs of our model. With a large number of future merger detections, we should be able to infer the black hole mass spectrum (e.g., [40]) and to confirm or rule out our PBH formation mechanism.

We also determined an upper bound on the mass of the largest PBH that one can expect to find in a large galaxy, $M_{\text{bh}} \lesssim 10^7 M_{\odot}$. This shows that PBHs of our model can serve as seeds of supermassive black holes (SMBH) observed at the galactic centers. There is

in fact a range of parameters for which the model can account for both SMBH and LIGO observations.

Black holes formed by vacuum bubbles can have significant observational effects only if the bubble nucleation rate is relatively high, $\lambda \sim 10^{-12} - 10^{-15}$. This corresponds to the tunneling action $S \sim 30$, while the typical value is $S \gtrsim 100$. We note, however, that in the string landscape scenario the false vacuum has a large number (~ 100) of decay channels, and it seems likely that some of them may have small barriers with a relatively high tunneling probability.

Our analysis in this paper is based on several simplifying assumptions. To begin with, we assumed that the vacuum energy is instantaneously thermalized at the end of inflation. In a more realistic model, thermalization may extend over several Hubble times and may be preceded by a period of the inflaton field oscillations characterized by the dust equation of state. We also assumed that the bubble radius at nucleation is much smaller than the Hubble horizon.

These assumptions, however, affect only the low-mass end of the black hole distribution, $M_{\text{bh}} \lesssim M_{\text{min}}$. Perhaps more consequential is the assumption that thermalized matter particles cannot penetrate the bubble and are reflected from the bubble wall. This is likely to be true for particles with energies lower than the symmetry breaking scale of the bubble, $\epsilon < \eta_b, \eta_\sigma$, but at higher energies the wall may be transparent to the particles [42].

We also assumed that the bubble wall tension σ and the bubble nucleation rate λ are constant parameters. However, this is not generally the case. When the bubble is formed, the wall tension is determined by the shape of the barrier between the inflating false vacuum of energy density ρ_i and the vacuum in the bubble interior of energy density ρ_b . On the other hand, at the end of inflation the barrier is between our vacuum of very low energy density and the bubble interior. This means that the shape of the barrier and the wall tension can change significantly in the course of inflation.

The bubble nucleation rate λ may also change during inflation. As the inflaton field rolls downhill, it moves relative to the minimum at ρ_b , so the tunneling path (and therefore the tunneling action) are also changing. As a result the mass distribution of black holes could be significantly modified and could develop a peak at the value of M_{bh} that corresponds to the smallest tunneling action. We leave the analysis of these possibilities for future research.

Acknowledgments

This work was supported by the National Science Foundation under grant 1518742. H.D. was also supported by Burlingame Fellowship at Tufts University. We are grateful to Jaume Garriga and Andrei Gruzinov for very useful discussions and to Vladyslav Syrotenko for his participation at the early stages of this project. We would also like to thank Bernard Carr for useful comments on the manuscript, and Xiaozhe Hu for helpful advice on some simulation issues.

Appendix A

In this appendix we use Israel's junction conditions to find the conditions needed for simulations. We closely follow the method and notation in [43].

The interior of the vacuum bubble can be described by de Sitter spacetime with metric

$$ds^2 = -dt_d^2 + a^2(dr_d^2 + r_d^2 d\Omega_2^2), \quad (\text{A1})$$

where $a(t_d) = H_b^{-1} \exp(H_b t_d)$ with H_b the Hubble constant. We assume that outside the bubble

$$ds^2 = -A^2 dt^2 + B^2 dr^2 + R^2 d\Omega_2^2, \quad (\text{A2})$$

where A , B and R are functions of t and r .

Let the trajectory of the wall be $(t_d(\tau), r_d(\tau))$ or $(t(\tau), r(\tau))$, where τ is the wall proper time. If the wall is comoving for an exterior observer, $\partial_\tau r = 0$, where $\partial_\tau \equiv d/d\tau$. The tangent vector to the wall hypersurface is $v^\mu = (\partial_\tau t, \partial_\tau r) = (\partial_\tau t, 0)$, and $v_\mu = (-A^2 \partial_\tau t, B^2 \partial_\tau r) = (-A^2 \partial_\tau t, 0)$. Assuming $\partial_\tau t$ to be positive, $v^\mu v_\mu = -1$ gives $\partial_\tau t = A^{-1}$. Let ξ^μ be a unit vector normal to the wall hypersurface; then $\xi^\mu v_\mu = 0$ and $\xi^\mu \xi_\mu = 1$, which give $\xi^\mu = (A^{-1} B \partial_\tau r, AB^{-1} \partial_\tau t) = (0, B^{-1})$ and $\xi_\mu = (0, B)$.

We define the brackets $[Q] \equiv Q_{\text{out}} - Q_{\text{in}}$, and $\{Q\} \equiv Q_{\text{out}} + Q_{\text{in}}$. Here "in" and "out" respectively denote the value of Q right inside and outside the wall. Then Israel's first junction condition is $[h_{\mu\nu}] = 0$, where $h_{\mu\nu}$ is the induced metric at the wall. The second junction condition is $[K_{\mu\nu}] = 8\pi(-S_{\mu\nu} + Sh_{\mu\nu}/2)$, where $K_{\mu\nu}$ is the extrinsic curvature at the wall, $S_{\mu\nu} = -\sigma h_{\mu\nu}$ is the energy-momentum tensor of the wall, with σ the surface energy density (or tension).

The equation of motion for the wall is given by

$$\left\{ \xi_\mu \frac{Dv^\mu}{d\tau} + 2\xi^\mu \partial_\mu \ln R \right\} = -\frac{2}{\sigma} [(\rho + p)(u^\mu \xi_\mu)^2 + p], \quad (\text{A3})$$

where u^μ is the 4-velocity of the fluid. Inside the bubble $\rho + p = 0$.

We shall now use the junction conditions and Eq.(A3) to derive some relations that will be useful for setting up the boundary condition for our simulations.

By the first junction condition, $ar_d = R$ at the wall. Taking the derivative of R with respect to τ gives

$$\partial_\tau R = \dot{R} \partial_\tau t + R' \partial_\tau r = \frac{\dot{R}}{A} \equiv U. \quad (\text{A4})$$

Let $V \equiv a \partial_\tau r_d$. Then U at the wall can be written as

$$U = \partial_\tau (ar_d) = r_d \partial_\tau a + a \partial_\tau r_d = H_b R \sqrt{1 + V^2} + V. \quad (\text{A5})$$

The (θ, θ) component of the second junction condition gives

$$[\xi^\mu \partial_\mu R] = -4\pi\sigma R. \quad (\text{A6})$$

Right outside the wall, we have

$$\xi^\mu \partial_\mu R|_{\text{out}} = \frac{R'}{B} \equiv \Gamma, \quad (\text{A7})$$

while

$$\xi^\mu \partial_\mu R|_{\text{in}} = H_b R V + \sqrt{1 + V^2}. \quad (\text{A8})$$

Then by Eq. (A6), Γ at the wall can be written as

$$\Gamma = H_b R V + \sqrt{1 + V^2} - 4\pi\sigma R. \quad (\text{A9})$$

The (τ, τ) component of the second junction condition gives

$$\left[\xi_\mu \frac{Dv^\mu}{d\tau} \right] = -4\pi\sigma, \quad (\text{A10})$$

where $Dv^\mu/d\tau = \partial_\tau v^\mu + \Gamma_{\lambda\sigma}^\mu v^\lambda v^\sigma$, with $\Gamma_{\lambda\sigma}^\mu$ the Christoffel symbols for the 4-spacetime. Right outside the wall,

$$\xi_\mu \frac{Dv^\mu}{d\tau} \Big|_{\text{out}} = B\Gamma_{00}^1 v^0 v^0 = \frac{A'}{AB}. \quad (\text{A11})$$

By Eqs. (A10) and (A11),

$$\frac{A'}{AB} - \xi_\mu \frac{Dv^\mu}{d\tau} \Big|_{\text{in}} = -4\pi\sigma. \quad (\text{A12})$$

On the other hand, by Eqs. (A3), (A6), (A7), (A8) and (A11), we have

$$\frac{A'}{AB} + \xi_\mu \frac{Dv^\mu}{d\tau} \Big|_{\text{in}} = -\frac{2}{\sigma} [p] - \frac{4\Gamma}{R} - 8\pi\sigma. \quad (\text{A13})$$

Combining Eqs. (A12) and (A13) gives

$$A' = -AB \left(\frac{[p]}{\sigma} + \frac{2\Gamma}{R} + 6\pi\sigma \right). \quad (\text{A14})$$

This is used as the boundary condition in the simulations.

We can also obtain an explicit form of the equation of motion for the wall. It can be shown that

$$\xi_\mu \frac{Dv^\mu}{d\tau} \Big|_{\text{in}} = \frac{\partial_\tau V}{\sqrt{1+V^2}} + H_b V. \quad (\text{A15})$$

Then by Eqs. (A9), (A12), (A13) and (A15), the equation of motion of the wall is

$$\frac{\partial_\tau V}{\sqrt{1+V^2}} = -3H_b V - \frac{2}{R} \sqrt{1+V^2} + 6\pi\sigma - \frac{[p]}{\sigma}. \quad (\text{A16})$$

Appendix B

Vacuum bubbles can deviate from spherical shape due to quantum fluctuations. The unperturbed worldsheet of the bubble wall is a $(2+1)$ -dimensional de Sitter space with a Hubble parameter

$$\tilde{H} = \epsilon/3\sigma, \quad (\text{B1})$$

where ϵ is the difference of vacuum energy densities outside and inside the bubble, $\epsilon = \rho_i - \rho_b$ and σ is the tension of the bubble wall. The magnitude of fluctuations of the bubble radius was estimated in Ref. [30]:

$$\delta R \approx \left(\frac{\tilde{H}}{3\pi^2\sigma} \right)^{1/2} = \frac{\sqrt{\epsilon}}{3\pi\sigma}. \quad (\text{B2})$$

As the bubble expands, δR remains constant, so the ratio $\delta R/R$ decreases and the bubble becomes more and more spherical. Here R is the bubble radius.

This analysis, however, did not account for gravitational effects. When the bubble radius gets larger than the de Sitter horizon of the exterior inflating universe, $R > H_i^{-1}$, we expect that the shape of the bubble "freezes" and it is conformally stretched afterwards.⁷ The shape fluctuations are then given by

$$\frac{\delta R}{R} \sim \frac{\sqrt{\epsilon} H_i}{3\pi\sigma}. \quad (\text{B3})$$

Assuming that $\epsilon \sim \rho_i$, this is of the order

$$\frac{\delta R}{R} \sim \frac{\rho_i}{\sigma M_{\text{Pl}}}. \quad (\text{B4})$$

Widrow [44] studied perturbations on collapsing domain walls and found that the fluctuation δR remains approximately constant in the course of collapse. We will show that this also holds for collapsing bubbles later in this Appendix.

A black hole is formed if $\delta R < 2GM_{\text{bh}}$. Let us first assume that the bubble energy at the moment of maximal expansion ($R = R_{\text{max}}$) is dominated by the interior vacuum energy,

$$M_{\text{bh}} \sim \rho_{\text{b}} R_{\text{max}}^3. \quad (\text{B5})$$

Requiring that $\delta R \lesssim GM_{\text{bh}}$, we have

$$\delta R \sim \frac{\rho_i}{\sigma M_{\text{Pl}}} R_{\text{max}} \lesssim G\rho_{\text{b}} R_{\text{max}}^3 \quad (\text{B6})$$

and

$$R_{\text{max}} \gtrsim \left(\frac{\rho_i M_{\text{Pl}}}{\rho_{\text{b}} \sigma} \right)^{1/2}. \quad (\text{B7})$$

Substituting this into (B5) we obtain

$$M_{\text{bh}} \gtrsim \rho_{\text{b}} \left(\frac{\rho_i M_{\text{Pl}}}{\rho_{\text{b}} \sigma} \right)^{3/2} \equiv M_F. \quad (\text{B8})$$

If ρ_i , ρ_{b} and σ are characterized by the same energy scale η , this gives

$$M_{\text{bh}} \gtrsim \frac{M_{\text{Pl}}^{3/2}}{\eta^{1/2}}. \quad (\text{B9})$$

This is a rather weak constraint. For example, if η is the electroweak scale, it gives $M_{\text{bh}} > 1$ kg. On the other hand, the cutoff mass M_F can be relatively large when $\rho_{\text{b}} \ll \rho_i$.

⁷ More exactly, we expect fluctuations of wavelength λ to freeze when λ gets larger than $1/H_i$. But here we are interested in the lowest multipoles, so λ is comparable to the bubble radius.

Bubble collapse

Let us now show that the evolution of perturbations on a collapsing bubble is similar to that on a collapsing domain wall.

Let us first consider collapse of a spherical bubble. We start with the conserved mass,

$$\mathcal{M}_b = \frac{4\pi}{3}\rho_b R^3 + 4\pi\sigma R^2 \sqrt{1 + \dot{R}^2 - H_b^2 R^2} - 8\pi^2 G \sigma^2 R^3, \quad (\text{B10})$$

where the overdot stands for a derivative with respect to proper time τ . Suppose the bubble is initially at rest, $\dot{R} = 0$, at the maximal expansion radius, $R = R_{\text{max}}$. We will be interested in the asymptotic behavior, when $R \ll R_{\text{max}}$.

In this regime, the terms proportional to R^3 on the right hand side of (B10) become negligible and $|\dot{R}| \gg 1$, so Eq. (B10) reduces to

$$\mathcal{M}_b \approx -4\pi\sigma R^2 \dot{R}, \quad (\text{B11})$$

where the "-" sign is chosen because we are considering the collapse.

The solution of Eq. (B11) is

$$R(\tau) = \left(-\frac{3\mathcal{M}_b\tau}{4\pi\sigma} \right)^{1/3}. \quad (\text{B12})$$

Here, we choose the origin of τ so that $\tau = 0$ at the moment of collapse; then $\tau < 0$ prior to the collapse. It follows from (B12) that the total proper time it takes for the bubble to collapse is

$$\tau \sim \frac{\sigma R_{\text{max}}^3}{\mathcal{M}_b} \lesssim \frac{\sigma}{\rho_b}. \quad (\text{B13})$$

Fluctuations on the collapsing bubble are described by a scalar field ϕ living at the bubble wall and satisfying the equation

$$-\nabla^2\phi + \left(\mathcal{R} - \frac{\rho_b^2}{\sigma^2} \right) \phi = 0. \quad (\text{B14})$$

The field has a tachyonic mass, $m_\phi^2 = -\rho_b^2/\sigma^2$, and a non-minimal coupling to the 3-curvature \mathcal{R} on the wall worldsheet,

$$\mathcal{R} = \frac{2}{R^2} \left(1 + \dot{R}^2 + 2R\ddot{R} \right). \quad (\text{B15})$$

The worldsheet metric can be written as

$$ds^2 = -d\tau^2 + R^2(\tau)d\Omega^2. \quad (\text{B16})$$

Then, with the solution (B12) the 3-curvature becomes

$$\mathcal{R} = \frac{2}{R^2} - \frac{2}{3\tau^2} \approx -\frac{2}{3\tau^2}, \quad (\text{B17})$$

where the last approximation applies for $R \ll R_{\text{max}}$.

The tachyonic mass could in principle lead to an instability. But the timescale for such an instability to develop is $\Delta\tau > |m_\phi|^{-1}$, and we see from (B13) that there is not enough time. In fact, the mass term in Eq. (B14) is negligible compared to the curvature term for $R \ll R_{\text{max}}$. Neglecting this term and using the approximation (B17), we rewrite Eq. (B14) as

$$\ddot{\phi} + \frac{2}{3\tau}\dot{\phi} - \frac{2}{3\tau^2}\phi = 0. \quad (\text{B18})$$

This has solutions $\phi \propto \tau^\alpha$ with $\alpha = 1, -2/3$. The dominant solution is

$$\phi \propto \tau^{-2/3} \propto R^{-2}. \quad (\text{B19})$$

It was shown in [29] that the rms fluctuation of the bubble wall δR is related to ϕ as $\delta R \sim \phi/\gamma$, where $\gamma \propto R^{-2}$ is the Lorentz factor of the wall. (The factor of γ accounts for the effect of Lorentz contraction of bubble fluctuations.) Then Eq. (B19) tells us that the fluctuation amplitude does not change in the course of collapse:

$$\delta R \approx \text{const.} \quad (\text{B20})$$

This agrees with the result obtained by Widrow [44] for collapsing domain walls. The agreement between the two cases is not surprising, since the vacuum energy density ρ_b becomes dynamically unimportant at $R \ll R_{\text{max}}$.

-
- [1] Ya. B. Zeldovich and I.D. Novikov, *Sov. Phys. Astron. J.* **10**, 602 (1967).
 - [2] S. Hawking, "Gravitationally collapsed objects of very low mass," *Mon. Not. Roy. Astron. Soc.* **152**, 75 (1971).
 - [3] B. J. Carr and S. W. Hawking, "Black holes in the early Universe," *Mon. Not. Roy. Astron. Soc.* **168**, 399 (1974).
 - [4] B. J. Carr and J. E. Lidsey, "Primordial black holes and generalized constraints on chaotic inflation," *Phys. Rev. D* **48**, 543 (1993).

- [5] J. García-Bellido, A. D. Linde and D. Wands, “Density perturbations and black hole formation in hybrid inflation,” *Phys. Rev. D* **54**, 6040 (1996) [astro-ph/9605094].
- [6] J. Yokoyama, “Formation of MACHO primordial black holes in inflationary cosmology,” *Astron. Astrophys.* **318**, 673 (1997) [astro-ph/9509027].
- [7] P. H. Frampton, M. Kawasaki, F. Takahashi and T. T. Yanagida, “Primordial Black Holes as All Dark Matter,” *JCAP* **1004**, 023 (2010) [arXiv:1001.2308 [hep-ph]].
- [8] S. Clesse and J. García-Bellido, “Massive Primordial Black Holes from Hybrid Inflation as Dark Matter and the seeds of Galaxies,” *Phys. Rev. D* **92**, no. 2, 023524 (2015) [arXiv:1501.07565 [astro-ph.CO]].
- [9] H. Kodama, M. Sasaki and K. Sato, “Abundance of Primordial Holes Produced by Cosmological First Order Phase Transition,” *Prog. Theor. Phys.* **68**, 1979 (1982).
- [10] K. Jedamzik and J. C. Niemeyer, “Primordial black hole formation during first order phase transitions,” *Phys. Rev. D* **59**, 124014 (1999) [astro-ph/9901293].
- [11] M. Y. Khlopov, R. V. Konoplich, S. G. Rubin and A. S. Sakharov, “First order phase transitions as a source of black holes in the early universe,” *Grav. Cosmol.* **2**, S1 (1999) [hep-ph/9912422].
- [12] S. W. Hawking, “Black Holes From Cosmic Strings,” *Phys. Lett. B* **231**, 237 (1989).
- [13] A. Polnarev and R. Zembowicz, “Formation of Primordial Black Holes by Cosmic Strings,” *Phys. Rev. D* **43**, 1106 (1991).
- [14] J. Garriga and A. Vilenkin, “Black holes from nucleating strings,” *Phys. Rev. D* **47**, 3265 (1993) [hep-ph/9208212].
- [15] M. Y. Khlopov, S. G. Rubin and A. S. Sakharov, “Primordial structure of massive black hole clusters,” *Astropart. Phys.* **23**, 265 (2005) [astro-ph/0401532].
- [16] J. Garriga, A. Vilenkin and J. Zhang, “Black holes and the multiverse,” *JCAP* **1602**, no. 02, 064 (2016) [arXiv:1512.01819 [hep-th]].
- [17] H. Deng, J. Garriga and A. Vilenkin, “Primordial black hole and wormhole formation by domain walls,” *JCAP* **1704**, no. 04, 050 (2017) [arXiv:1612.03753 [gr-qc]].
- [18] S. R. Coleman and F. De Luccia, “Gravitational Effects on and of Vacuum Decay,” *Phys. Rev. D* **21**, 3305 (1980).
- [19] V. A. Berezhin, V. A. Kuzmin and I. I. Tkachev, “Thin Wall Vacuum Domains Evolution,” *Phys. Lett. B* **120**, 91 (1983).
- [20] S. K. Blau, E. I. Guendelman and A. H. Guth, “The Dynamics of False Vacuum Bubbles,”

- Phys. Rev. D **35**, 1747 (1987).
- [21] J. Bloomfield, D. Bulhosa and S. Face, “Formalism for Primordial Black Hole Formation in Spherical Symmetry,” arXiv:1504.02071 [gr-qc].
- [22] C. W. Misner and D. H. Sharp, “Relativistic equations for adiabatic, spherically symmetric gravitational collapse,” Phys. Rev. **136**, B571 (1964).
- [23] S. A. Hayward, “Gravitational energy in spherical symmetry,” Phys. Rev. D **53**, 1938 (1996) [gr-qc/9408002].
- [24] V. Faraoni, “Cosmological and black hole apparent horizons,” Vol. 907. Springer (2015).
- [25] T. W. Baumgarte and S. L. Shapiro, “Numerical relativity: solving Einstein’s equations on the computer,” Cambridge University Press (2010).
- [26] M. Liebendoerfer, S. Rosswog and F. K. Thielemann, “An Adaptive grid, implicit code for spherically symmetric, general relativistic hydrodynamics in comoving coordinates,” Astrophys. J. Suppl. **141**, 229 (2002) [astro-ph/0106539].
- [27] J. Von Neumann and R. Richtmyer, “A method for the numerical calculation of hydrodynamic shocks,” J. Appl. Phys. **21**, no. 3 (1950).
- [28] B. J. Carr, “The Primordial black hole mass spectrum,” Astrophys. J. **201**, 1 (1975).
- [29] J. Garriga and A. Vilenkin, “Perturbations on domain walls and strings: A Covariant theory,” Phys. Rev. D **44**, 1007 (1991).
- [30] J. Garriga and A. Vilenkin, “Quantum fluctuations on domain walls, strings and vacuum bubbles,” Phys. Rev. D **45**, 3469 (1992).
- [31] K. Hotokezaka and T. Piran, “Are the observed black hole mergers spins consistent with field binary progenitors?,” arXiv:1707.08978 [astro-ph.HE].
- [32] K. Inomata, M. Kawasaki, K. Mukaida, Y. Tada and T. T. Yanagida, “Inflationary primordial black holes for the LIGO gravitational wave events and pulsar timing array experiments,” Phys. Rev. D **95**, no. 12, 123510 (2017) [arXiv:1611.06130 [astro-ph.CO]].
- [33] J. García-Bellido, M. Peloso and C. Unal, “Gravitational Wave signatures of inflationary models from Primordial Black Hole Dark Matter,” arXiv:1707.02441 [astro-ph.CO].
- [34] B. Carr, F. Kühnel and M. Sandstad, “Primordial Black Holes as Dark Matter,” Phys. Rev. D **94**, no. 8, 083504 (2016) [arXiv:1607.06077 [astro-ph.CO]].
- [35] F. Kühnel and K. Freese, “Constraints on Primordial Black Holes with Extended Mass Functions,” Phys. Rev. D **95**, no. 8, 083508 (2017) [arXiv:1701.07223 [astro-ph.CO]].

- [36] B. Carr, M. Raidal, T. Tenkanen, V. Vaskonen and H. Veermäe, “Primordial black hole constraints for extended mass functions,” *Phys. Rev. D* **96**, no. 2, 023514 (2017) [arXiv:1705.05567 [astro-ph.CO]].
- [37] M. Sasaki, T. Suyama, T. Tanaka and S. Yokoyama, “Primordial Black Hole Scenario for the Gravitational-Wave Event GW150914,” *Phys. Rev. Lett.* **117**, no. 6, 061101 (2016) [arXiv:1603.08338 [astro-ph.CO]].
- [38] S. Bird, I. Cholis, J. B. Muñoz, Y. Ali-Haïmoud, M. Kamionkowski, E. D. Kovetz, A. Raccanelli and A. G. Riess, “Did LIGO detect dark matter?,” *Phys. Rev. Lett.* **116**, no. 20, 201301 (2016) [arXiv:1603.00464 [astro-ph.CO]].
- [39] Y. Ali-Haïmoud, E. D. Kovetz and M. Kamionkowski, “The merger rate of primordial-black-hole binaries,” arXiv:1709.06576 [astro-ph.CO].
- [40] M. Zevin, C. Pankow, C. L. Rodriguez, L. Sampson, E. Chase, V. Kalogera and F. A. Rasio, “Constraining Formation Models of Binary Black Holes with Gravitational-Wave Observations,” *Astrophys. J.* **846**, no. 1, 82 (2017) [arXiv:1704.07379 [astro-ph.HE]].
- [41] N. Duechting, “Supermassive black holes from primordial black hole seeds,” *Phys. Rev. D* **70**, 064015 (2004) [astro-ph/0406260].
- [42] A. E. Everett, “Observational consequences of a ‘domain’ structure of the universe,” *Phys. Rev. D* **10**, 3161 (1974).
- [43] N. Tanahashi and C. M. Yoo, “Spherical Domain Wall Collapse in a Dust Universe,” *Class. Quant. Grav.* **32**, no. 15, 155003 (2015) [arXiv:1411.7479 [gr-qc]].
- [44] L. M. Widrow, “The Collapse of Nearly Spherical Domain Walls,” *Phys. Rev. D* **39**, 3576 (1989).

This figure "0001.jpg" is available in "jpg" format from:

<http://arxiv.org/ps/1710.02865v2>

This figure "B.png" is available in "png" format from:

<http://arxiv.org/ps/1710.02865v2>

This figure "M-R.png" is available in "png" format from:

<http://arxiv.org/ps/1710.02865v2>

This figure "MF.png" is available in "png" format from:

<http://arxiv.org/ps/1710.02865v2>

This figure "M_t.png" is available in "png" format from:

<http://arxiv.org/ps/1710.02865v2>

This figure "PBH_new.png" is available in "png" format from:

<http://arxiv.org/ps/1710.02865v2>

This figure "PBHplot.png" is available in "png" format from:

<http://arxiv.org/ps/1710.02865v2>

This figure "R-r.png" is available in "png" format from:

<http://arxiv.org/ps/1710.02865v2>

This figure "R.png" is available in "png" format from:

<http://arxiv.org/ps/1710.02865v2>

This figure "delrho.png" is available in "png" format from:

<http://arxiv.org/ps/1710.02865v2>

This figure "rho-r.png" is available in "png" format from:

<http://arxiv.org/ps/1710.02865v2>

This figure "rho-r1.png" is available in "png" format from:

<http://arxiv.org/ps/1710.02865v2>

This figure "rho1.png" is available in "png" format from:

<http://arxiv.org/ps/1710.02865v2>

This figure "rho-r2.png" is available in "png" format from:

<http://arxiv.org/ps/1710.02865v2>

This figure "rho2.png" is available in "png" format from:

<http://arxiv.org/ps/1710.02865v2>

This figure "rho-r4.png" is available in "png" format from:

<http://arxiv.org/ps/1710.02865v2>

This figure "sub.png" is available in "png" format from:

<http://arxiv.org/ps/1710.02865v2>

This figure "sup.png" is available in "png" format from:

<http://arxiv.org/ps/1710.02865v2>